Joule

Article

Gel electrolyte featuring parasitic salt-phobic network enables anode-free lithium batteries with long cycle life and enhanced thermal stability

Graphical abstract

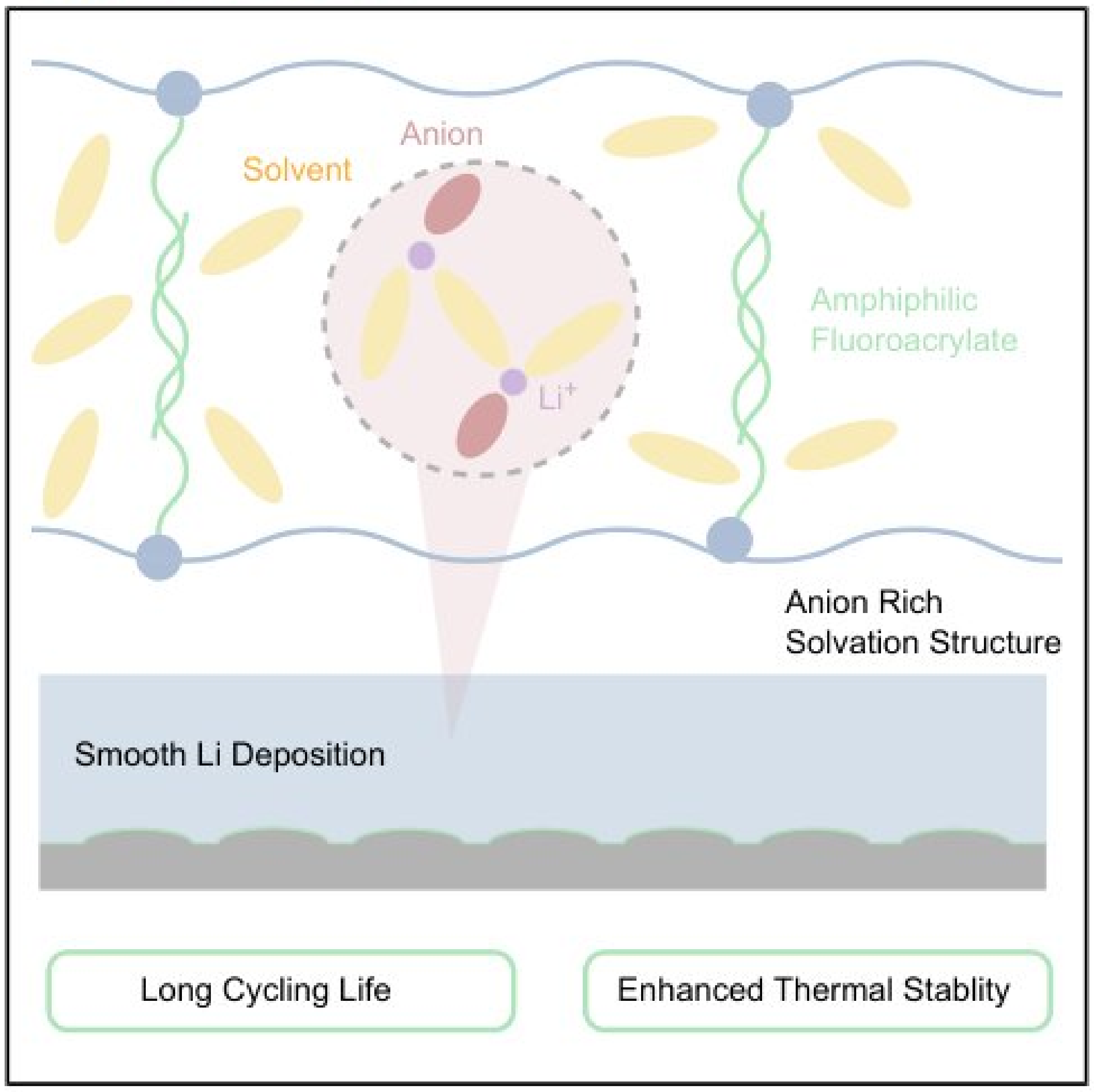

Highlights

- A parasitic salt-phobic network is constructed in the gel polymer electrolyte
- Such a network attracts solvents but repels salts, enabling anion-rich solvation
- Anode-free pouch cell shows excellent cycling life and enhanced thermal stability

Authors

Shengyu Cong, Zhenghao Yang, Xuhao Wan, ..., Seung Woo Lee, Yongseok Kim, Yuan Yang

Correspondence

yy2664@columbia.edu

In brief

Advancing safe and durable lithium batteries requires clearer insight into how electrolytes govern ion behavior. This work demonstrates that rational polymer design can reshape lithium-ion solvation, a largely overlooked lever in battery optimization. By engineering a gel electrolyte that promotes a stable anion-rich environment, the work enables improved cycling stability and thermal stability in anode-free cells. These findings highlight the importance of molecular-level solvation control and offer a practical strategy for next-generation high-energy batteries.

Cong et al., 2026, Joule *10*, 102296
April 15, 2026
https://doi.org/10.1016/j.joule.2025.102296

CellPress

Please cite this article in press as: Cong et al., Gel electrolyte featuring parasitic salt-phobic network enables anode-free lithium batteries with long cycle life and enhanced thermal stability, Joule (2025), https://doi.org/10.1016/j.joule.2025.102296

Joule

CellPress

Article

Gel electrolyte featuring parasitic salt-phobic network enables anode-free lithium batteries with long cycle life and enhanced thermal stability

Shengyu Cong,[1,6] Zhenghao Yang,[1,6] Xuhao Wan,[2,6] Han Chen,[1] Shiyi Yuan,[1] Zhihao Yang,[1] Yuchen Yang,[1] Tong Wang,[3] Sheng Zhang,[3] Maya Narayanan Nair,[3] Yuzheng Guo,[2] Yuanyuan Ma,[4] Yang Li,[4] Hyunsik Woo,[5] Seung Woo Lee,[5] Yongseok Kim,[4] and Yuan Yang[1,7,*]

[1]Department of Applied Physics and Applied Mathematics, Columbia University, New York, NY 10027, USA
[2]School of Electrical Engineering and Automation, Wuhan University, Wuhan, China
[3]Advanced Science Research Center at the Graduate Center, City University of New York, New York, NY 10031, US
[4]Samsung SDI R&D America (SDIRA), Cambridge, MA 02138, USA
[5]Next Generation Development Group, Samsung SDI Research Center, Suwon-si 16678, Gyeonggi-do, Republic of Korea
[6]These authors contributed equally
[7]Lead contact
*Correspondence: yy2664@columbia.edu

https://doi.org/10.1016/j.joule.2025.102296

CONTEXT & SCALE Gel polymer electrolytes are promising for lithium batteries due to their high ionic conductivity, excellent thermal stability, unique rigid-flexible frameworks, and favorable chemical compatibility with lithium metal. Despite these advances, the fundamental relationship between polymer backbone chemistry and lithium-ion solvation and transport remains poorly understood, and the intrinsic role of the polymer framework in regulating Li^+ solvation structure has often been overlooked. In this work, we design an *in situ* fluoroacrylate-based gel polymer electrolyte featuring a parasitic salt-phobic network that successfully promotes an anion-rich solvation structure, enabling both extended cycling life and enhanced thermal stability in an anode-free lithium battery. The secondary salt-phobic networks within the polymer matrix act as nanoscale domain walls that attract solvents but repel lithium salts, thereby inducing chemical inhomogeneity in the electrolyte and promoting anion-rich solvation of Li^+ ions due to the reduced availability of nearby solvent molecules. Importantly, the anion-rich solvation structure is confirmed by Raman spectroscopy, nuclear magnetic resonance, and molecular dynamics simulations. Moreover, such a tailored solvation environment promotes an anion-derived solid electrolyte interphase that effectively stabilizes lithium plating/stripping and mitigates interfacial parasitic reactions. The parasitic salt-phobic network design not only deepens the mechanistic understanding of solvation chemistry for polymer electrolytes in anode-free systems but also provides a practical pathway toward next-generation safe and durable energy storage systems.

SUMMARY

Anode-free lithium metal batteries offer high energy density but suffer from poor cycle life and thermal instability due to unstable anode morphology and parasitic interfacial reactions. We address these challenges by developing a gel polymer electrolyte featuring a parasitic salt-phobic network. Copolymerization of a branched acrylate and a fluoroacrylate forms the primary gel matrix, while fluoroacrylate-driven interchain interactions induce a secondary network that attracts solvents but excludes salts, creating nanoscale compositional inhomogeneity and promoting anion-rich solvation. This regulated microstructure enhances Li deposition/stripping reversibility, cycling life, and thermal stability. In 4.8 mAh/cm^2 Cu/NCA pouch cells, 80.3% of the initial 192.2 mAh/g is retained after 100 cycles, while 240 mAh anode-free cells maintain 81.2% after 70 cycles with 2.8 g/Ah electrolyte at 3.0–4.3 V and exhibit no thermal runaway in drilling tests. This work highlights polymer backbone chemistry as a powerful handle for tuning solvation and enabling safe, high-energy anode-free batteries.

Please cite this article in press as: Cong et al., Gel electrolyte featuring parasitic salt-phobic network enables anode-free lithium batteries with long cycle life and enhanced thermal stability, Joule (2025), https://doi.org/10.1016/j.joule.2025.102296

INTRODUCTION

Lithium metal batteries (LMBs) are attractive for next-generation energy storage, given the ultrahigh specific capacity of lithium metal anode.[1–3] However, lithium metal is costly and difficult to process since it is highly air sensitive.[4,5] In addition, the high ductility of lithium metal causes contamination in electrode slicing, increasing complications in cell manufacturing.[6,7] In principle, a lithium metal anode is not needed since the mainstream cathodes contain enough lithium ions for cycling.[8,9] This fact leads to the so-called "anode-free" LMBs with the structure of Cu/separator/cathode/Al.[10–12] Such a design allows for maximizing the energy density for a given cathode.[13,14] For example, anode-free cells employing a $LiNi_{1-x-y}Co_xAl_yO_2$ (NCA) cathode exhibit 24% and 78% higher volumetric energy density than LMBs and lithium-ion batteries, respectively (Figure 1A; Table S1).

Despite these advantages, anode-free LMBs face substantial challenges. First, the cycle life is limited by the continuous loss of active lithium, originating from poor solid electrolyte interphase (SEI) and thus inhomogeneous lithium deposition.[15,16] Besides, a pressure higher than 1.0 MPa is often needed for improving the cycling life, whereas a pressure below 0.8 MPa is highly desirable for practical applications.[17] Moreover, safety remains another concern, particularly with flammable electrolytes and high Ni-oxide cathodes.[18–20]

Anion-rich solvation has emerged as a promising strategy to stabilize lithium metal anodes by forming a salt-anion-derived SEI (e.g., LiF and Li_2O) that ensures uniform lithium nucleation and growth and mitigates electrolyte depletion.[3,21–23] To date, scientists primarily focus on localized high-concentration electrolytes (LHCEs) to achieve anion-rich solvation. In LHCEs (Figure 1B), a high salt-to-solvent ratio (SSR) ensures anion-rich

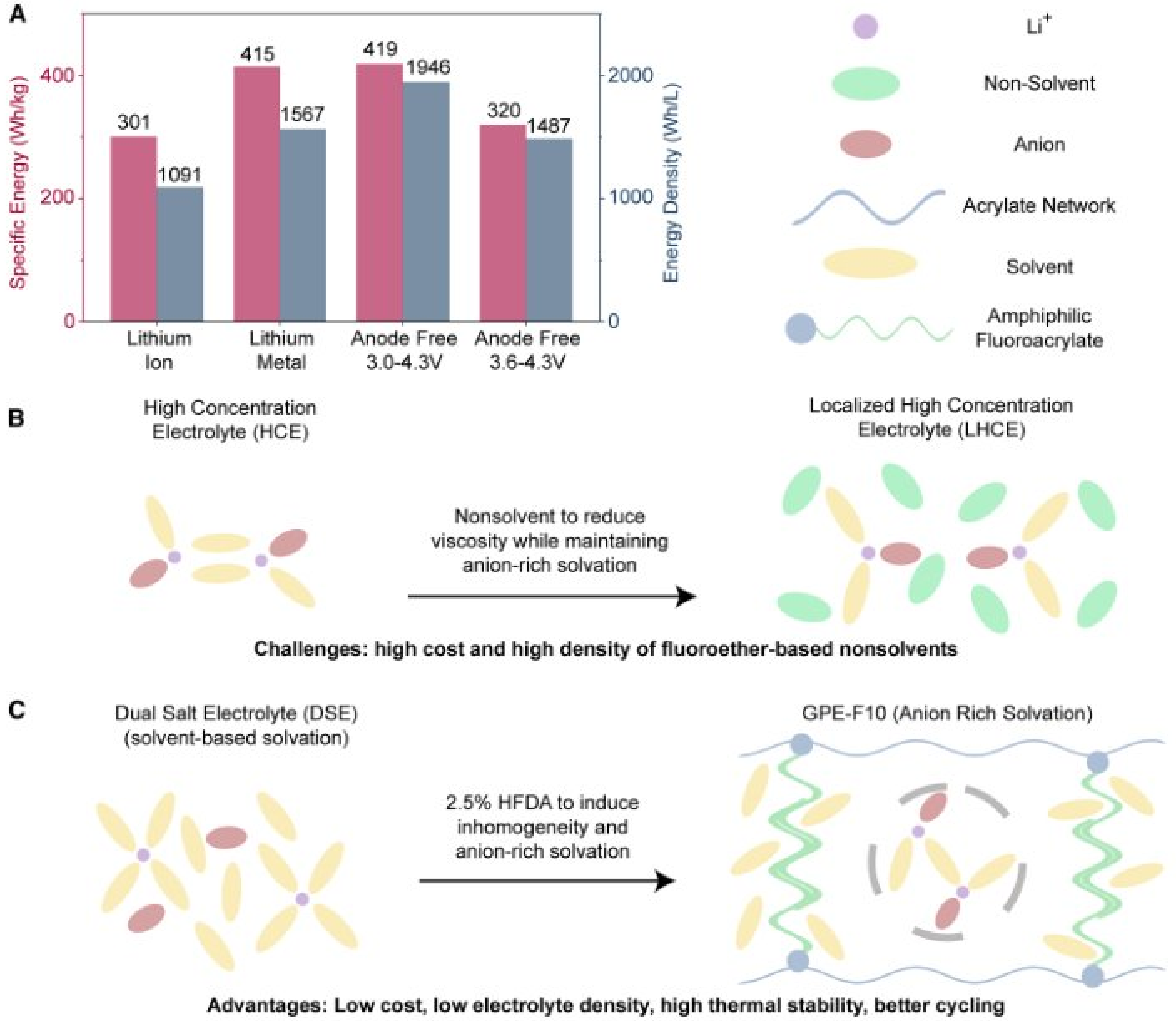

Figure 1. Design concept of polymer gel matrix featuring a parasitic salt-phobic network

(A) Calculated energy density and specific energy of graphite/NCA, Li/NCA, and Cu/NCA anode-free batteries. The area-specific capacity for NCA is 4.8 mAh/cm^2. Details can be found in Tables S1 and S5.

(B) Conventional LHCEs rely on large amounts (>60 wt %) of fluorinated nonsolvents, which increase cost and electrolyte density, posing challenges for practical implementation.

(C) Gel polymer matrix with a parasitic salt-phobic network generated by the interchain interactions of 2.5 wt % fluoroacrylate, promoting an anion-rich solvation structure.

Please cite this article in press as: Cong et al., Gel electrolyte featuring parasitic salt-phobic network enables anode-free lithium batteries with long cycle life and enhanced thermal stability, Joule (2025), https://doi.org/10.1016/j.joule.2025.102296

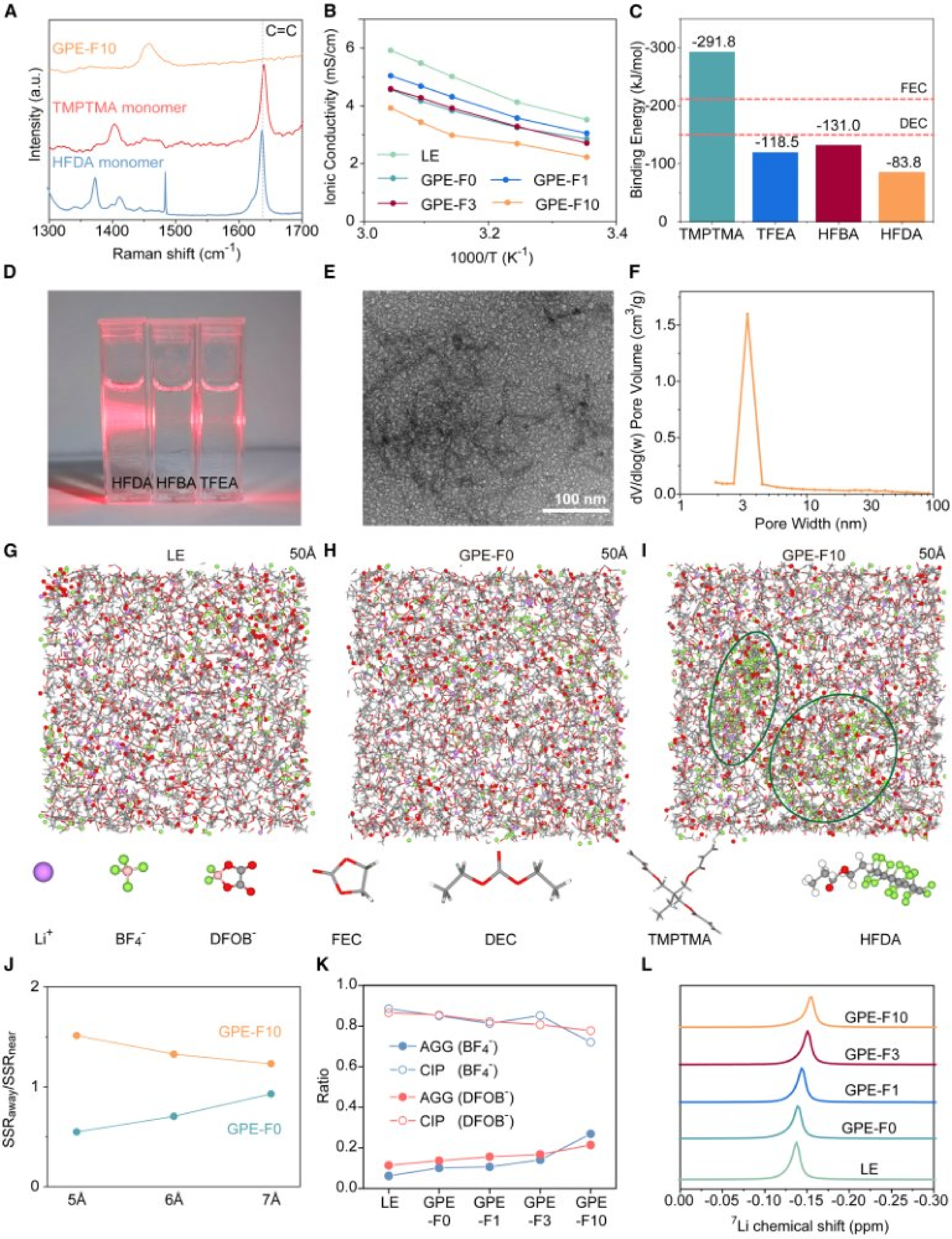

(legend on next page)

Please cite this article in press as: Cong et al., Gel electrolyte featuring parasitic salt-phobic network enables anode-free lithium batteries with long cycle life and enhanced thermal stability, Joule (2025), https://doi.org/10.1016/j.joule.2025.102296

solvation, and the heavily fluorinated nonsolvent lowers viscosity.[24–26] However, the high content of fluorinated nonsolvents (>60 wt %) significantly increases cost, environmental concerns, and electrolyte density, reducing the energy density at the cell level.[27,28] Therefore, the development of advanced electrolytes that enable anion-rich solvation while minimizing fluorinated diluents is highly desirable.

This work proposes a design strategy to enable anion-rich solvation by spatially segregating solvent-rich domains from Li^+ solvation sites in the electrolyte (Figure 1C). Specifically, a gel polymer electrolyte featuring a parasitic salt-phobic fluoropolymer network is developed. In this electrolyte, branched acrylates construct the primary gel polymer matrix, while only 2.5 wt % fluoroacrylate is covalently incorporated via its acrylate head. Notably, the salt-phobic fluorocarbon tails self-assemble through interchain interactions, forming a secondary parasitic network that spatially segments the electrolyte into nanoscale domains (< 5 nm). The parasitic salt-phobic network, which acts as nanoscale domain walls, exhibits high affinity toward solvents but repels lithium salts, further creating chemical inhomogeneity in the electrolyte phase, promoting anion-rich solvation among Li^+ ions due to the presence of less solvent around them. Such a design offers the following advantages over conventional LHCEs: (1) the parasitic salt-phobic network can precisely regulate Li^+ solvation by selectively coordinating solvents while excluding salts. Such a well-defined anion-rich solvation promotes the formation of a robust, high-quality SEI. By contrast, nonsolvents in conventional LHCEs have limited tunability over the solvation structure. (2) The polymer phase substantially enhances thermal stability, whereas LHCEs have limited thermal stability (Figure S1), and (3) owing to the low content of fluorinated acrylate (2.5 wt %), the overall gel electrolyte cost is considerably lower than that of LHCEs, which often contain a large fraction of expensive fluoroethers (Table S2). Furthermore, such a design exhibits a reduced electrolyte density of 1.27 g/cm^3, compared with ~1.51 g/cm^3 for typical LHCEs (Table S2), which can help increase the energy density of cells.

Based on this design concept, trimethylolpropane trimethacrylate (TMPTMA) and heneicosafluorododecyl acrylate (HFDA) are used to form such a gel polymer electrolyte. Raman, NMR, cryogenic transmission electron microscopy (cryo-TEM), and X-ray photoelectron spectroscopy (XPS) characterizations validate anion-rich solvation and LiF-rich SEI. With this electrolyte, Cu/NCA multilayer pouch cells deliver an initial capacity of 196.5 mAh/g and retain 81.2% after 70 cycles at 3.0–4.3 V under harsh conditions (2.8 g electrolyte/Ah, 0.7 MPa, and 4.8 mAh/cm^2, 0.2C/0.5C charge/discharge). With a narrower voltage range of 3.4–4.3 and 3.6–4.3 V, the capacity retention is further improved to 80.3%/100 cycles and 87.2%/200 cycles, respectively. Such performance is better or on par with the best reported results. Moreover, these pouch cells show excellent thermal stability and pass the rigorous drilling test at the fully charged state without thermal runaway.

RESULTS

Design of a gel polymer matrix featuring parasitic salt-phobic network

To realize the proposed gel electrolyte design, we selected TMPTMA as the backbone, as its branch structure can form a polymer network at a low concentration (e.g., 3%–5%), which does not compromise the ionic conductivity significantly.[29] The parasitic salt-phobic network is based on HFDA. Moreover, to understand the effectiveness of the design, we studied gel electrolyte with a series of fluoroacrylate monomers with different lengths of CF_x chains: 5 wt % TMPTMA (no CF_x group, denoted as GPE-F0), 2.5 wt % TMPTMA + 2.5 wt % 2,2,2-trifluoroethyl acrylate (TFEA) (-CF_3 group, GPE-F1), 2.5 wt % TMPTMA + 2.5 wt % 2,2,3,4,4,4-hexafluorobutyl acrylate (HFBA) (-C_3F_6 group, GPE-F3), and 2.5 wt % TMPTMA + 2.5 wt % HFDA (-$C_{10}F_{21}$ group, GPE-F10). The liquid phase is always 1.0 M LiDFOB + 0.4 M $LiBF_4$ in diethyl carbonate (DEC)/fluoroethylene carbonate (FEC) (2:1, by volume, denoted as LE) since it leads to one of the best-performing anode-free batteries.[10]

A scheme of preparation of gel electrolytes is shown in Figure S2. All four polymer gel electrolytes above were prepared by polymerizing LE with corresponding monomers and initiator at 55°C for 12 h (Figure S3). Raman spectroscopy confirms

Figure 2. Gel polymer electrolytes and their physical properties

(A) Raman spectra of monomers and GPE-F10, showing that monomers are completely polymerized in GPE-F10.

(B) Dependence of the intrinsic ionic conductivities of the electrolytes as a function of temperature.

(C) Binding energy between Li^+ and acrylate monomers calculated by DFT. Dashed lines indicate the binding energy between Li^+ and corresponding solvent molecules. HFDA has the smallest binding energy, which means the highest salt-phobic nature.

(D) Laser beam scattering tests for 2.5 wt % fluorinated acrylates in the liquid electrolyte (left to right: HFDA, HFBA, and TFEA). Only HFDA shows strong scattering, indicating the existence of a micelle.

(E) Cryo-TEM image of GPE-F10 after gelation, showing the aggregation of fluoroacrylate molecules and their participation in the gel matrix after gelation. The voltage is 200 kV. The magnification is 300,000.

(F) Barrett–Joyner–Halenda (BJH)desorption pore size distribution of GPE-F10 after freeze drying, fundamentally modifying the nanoporous architecture of the gel matrix by the parasitic network.

(G–I) MD-simulated structures of (G) LE, (H) GPE-F0, and (I) GPE-F10, with the two green circles showing the interchain interactions and aggregation of the HFDA molecule.

(J) MD-simulated salt-to-solvent ratio (SSR) profiles for GPE-F0 and GPE-F10. SSR_{away} (xÅ) is defined as SSR in regions more than x Å away from polymer molecules inside, and SSR_{near} (xÅ) is defined as SSR in regions within x Å away from polymer molecules, so $SSR_{away}/SSR_{near} > 1$ in GPE-F10 means that it is salt-phobic, driving the formation of an anion-rich solvation structure in GPE-F10.

(K) Raman spectra analysis of $DFOB^-$ and BF_4^- anions with LiDFOB and $LiBF_4$ dissolved in various electrolytes. GPE-F10 shows a more anion-rich solvation structure.

(L) Comparison of ^7Li NMR spectra of electrolytes in the liquid state, referenced to 0.1 M LiCl in H_2O. The upfield trend shows stronger interaction between the anions and Li^+ is observed in GPE-F10.

Please cite this article in press as: Cong et al., Gel electrolyte featuring parasitic salt-phobic network enables anode-free lithium batteries with long cycle life and enhanced thermal stability, Joule (2025), https://doi.org/10.1016/j.joule.2025.102296

that the C=C bonds at ~1,640 cm^{-1} diminish after heating, indicating complete polymerization (Figures 2A and S4).[30,31] Fourier transform infrared (FTIR) pectroscopy and X-ray diffraction (XRD) analyses (Figures S5 and S6) confirm the successful incorporation of fluorinated units and the predominantly amorphous nature of the gel polymer electrolytes, which are features that are favorable for efficient lithium-ion transport.[32,33] Ionic conductivities of these electrolytes are measured by impedance in a stainless steel symmetric cell configuration. GPE-F0, GPE-F1, GPE-F3, and GPE-F10 show ionic conductivities of 2.9, 3.0, 2.7, and 2.2 mS/cm at 25°C, respectively, which are close to LE (3.5 mS/cm; Figure 2B), validating that a small portion of TMPTMA can form gel electrolytes without substantially sacrificing ionic conductivity. The temperature-dependent conductivity between 25°C and 55°C shows the same trend as results at room temperature (LE > GPE-F0 ≈ GPE-F1 ≈ GPE-F3 > GPE-F10) (Figures 2B and S7). Moreover, the reported gels maintain an average electrolyte retention of 99.1% and an ionic conductivity retention of 99.0% relative to the freshly prepared samples (Figure S8), demonstrating an excellent stability with a shelf life of at least 7 days.[34,35] Besides, compression tests of the gel polymers (Figure S9) reveal that GPE-F0 exhibits the highest modulus (34.7 kPa) due to its high crosslinking density, whereas GPE-F1, GPE-F3, and GPE-F10 show lower values (~9–10 kPa).

Density functional theory (DFT) calculation shows that fluoroacrylate with a longer CFx chain leads to weaker binding between Li^+ and the polymer phase, thus showing a more salt-phobic nature. The binding energy (E_b) between Li^+ and monomers increases from −291.8 kJ/mol for TMPTMA to −118.5, −130.9, and −83.8 kJ/mol for TFEA, HFBA, and HFDA, respectively (Figure 2C). Hence, a long perfluorinated chain in HFDA promotes the repulsion between the polymer phase and the liquid electrolyte.[36–38] After confirming the salt-phobic nature of long-fluorocarbon chains, the aggregation behavior of fluoroacrylate is further investigated. A typical micelle behavior of HFDA in liquid electrolyte is observed in the Tyndall effect test (Figure 2D), and a corresponding micelle size of 120 nm is found by dynamic light scattering (DLS) (Figure S10). These results highlight the salt-phobic nature of HFDA and demonstrate the aggregation of its salt-phobic tails via interchain interactions in the electrolyte.[39] By contrast, no micelle formation is observed for TFEA and HFBA (Figure 2D), which is attributed to their shorter fluorocarbon chains.

Further, the participation of fluoroacrylate in the polymer matrix can be shown by cryo-TEM. GPE-F10 exhibits aggregation behavior before gelation (Figure S11), consistent with the Tyndall effect test. After gelation, a cross-linked polymer network is observed, indicating that HFDA has been integrated into the network (Figure 2E). Importantly, such interchain interactions from fluorocarbon segments of HFDA in the liquid electrolyte are retained within the gel matrix. As expected, molecular dynamics (MD) simulations reveal the aggregation behavior in GPE-F10 (Figure 2I), driven by interchain interactions among the fluorocarbon chains, while no such interchain interactions are observed in LE and GPE-F0 (Figures 2G and 2H). It is rationally hypothesized that these interchain interactions in GPE-F10 can form a secondary parasitic network, thus spatially confining electrolyte into nanoscale domains and thereby promoting the formation of an anion-rich solvation structure.

To validate this hypothesis, nitrogen adsorption-desorption measurements are applied to confirm the formation of a parasitic network in GPE-F10. Nitrogen adsorption-desorption measurements reveal that the structure of GPE-F10 after freeze drying is predominantly composed of highly uniform nanopores (Figures 2F and S12). The freeze-dried GPE-F10 exhibits a high Brunauer–Emmett–Teller (BET) specific surface area of 368 m^2/g and an average pore diameter of 3.7 nm. However, a much lower specific surface area (116 m^2/g) and a higher but more heterogeneous pore diameter (6.8 nm) are found in GPE-F3 (Figure S12). These distinctions provide strong evidence for the emergence of a secondary parasitic network, which fundamentally modifies the nanoporous architecture of the gel matrix. Scanning electron microscopy (SEM) analysis also reveals that GPE-F10 exhibits a finely segmented, nanoscale pore structure, whereas GPE-F3 displays larger, more heterogeneous nanopores (Figure S13). SEM observations are consistent with BET measurements, both indicating the formation of a secondary parasitic network in GPE-F10.

Furthermore, the salt-phobic polymer network can result in a higher concentration of salt in regions away from the polymer network. This is first supported by MD simulations (Figure 2J), where GPE-F10 shows a higher SSR in regions away from the polymer network, which promotes anion-rich solvation. By contrast, GPE-F0 shows a low SSR in regions away from the polymer network. Consistently, the polymer phase in GPE-F10 (HFDA + TMPTMA) leads to the largest difference in contact angle (16.5°) between the dual-salt electrolyte (LiDFOB/$LiBF_4$ in FEC/DEC) and the corresponding pure solvent (FEC/DEC), much larger than polymers in GPE-F0 (1.5°), GPE-F1 (3.3°), and GPE-F3 (5.6°) (Figures S14 and S15). Such results further validate the salt-phobic nature of HFDA.

Then, Raman spectroscopy is used to study Li^+ solvation in various electrolytes (Figures 2K and S16). By deconvolving Raman spectra for anions (BF_4^- and $DFOB^-$), it is found that the percentage of ion-aggregated (AGG) anions increases with a longer fluorocarbon chain, as discussed in Note S1. Notably, GPE-F10 exhibited the highest AGG portion in both BF_4^- and $DFOB^-$ anions among LE and gel electrolytes. As a higher AGG portion indicates an anion-rich solvation structure,[40–42] such results strongly corroborate our hypothesis that a parasitic salt-phobic network can promote anions prevailing to coordinate with Li^+. Besides, GPE-F10 displays a more negative ^{7}Li chemical shift (−0.156 ppm) than LE (−0.138 ppm) and other gel electrolytes (−0.139 ppm for GPE-F0, −0.143 ppm for GPE-F1, −0.150 ppm for GPE-F3) in Figure 2L. Compared with other electrolytes, the more upfield shift of GPE-F10 demonstrates the increase in electron density around Li^+, which results in a relatively strong shielding of Li^+, indicating the stronger interaction between the anions and Li^+.[43,44] The same trend was also observed in fluoroacrylates alone to eliminate the influence of TMPTMA in Figure S17. The formation of an anion-rich solvation structure driven by a parasitic network is further deciphered by calculating the radial distribution functions (RDFs) and cumulative distribution functions (CDFs) using MD simulations (Figure S18). GPE-F10 shows a lower Li–O (DEC) and Li–O (FEC) frequency (the absolute value of g[r]) than LE and GPE-F0, demonstrating that the solvents are less likely to enter the first solvation sheath of

Please cite this article in press as: Cong et al., Gel electrolyte featuring parasitic salt-phobic network enables anode-free lithium batteries with long cycle life and enhanced thermal stability, Joule (2025), https://doi.org/10.1016/j.joule.2025.102296

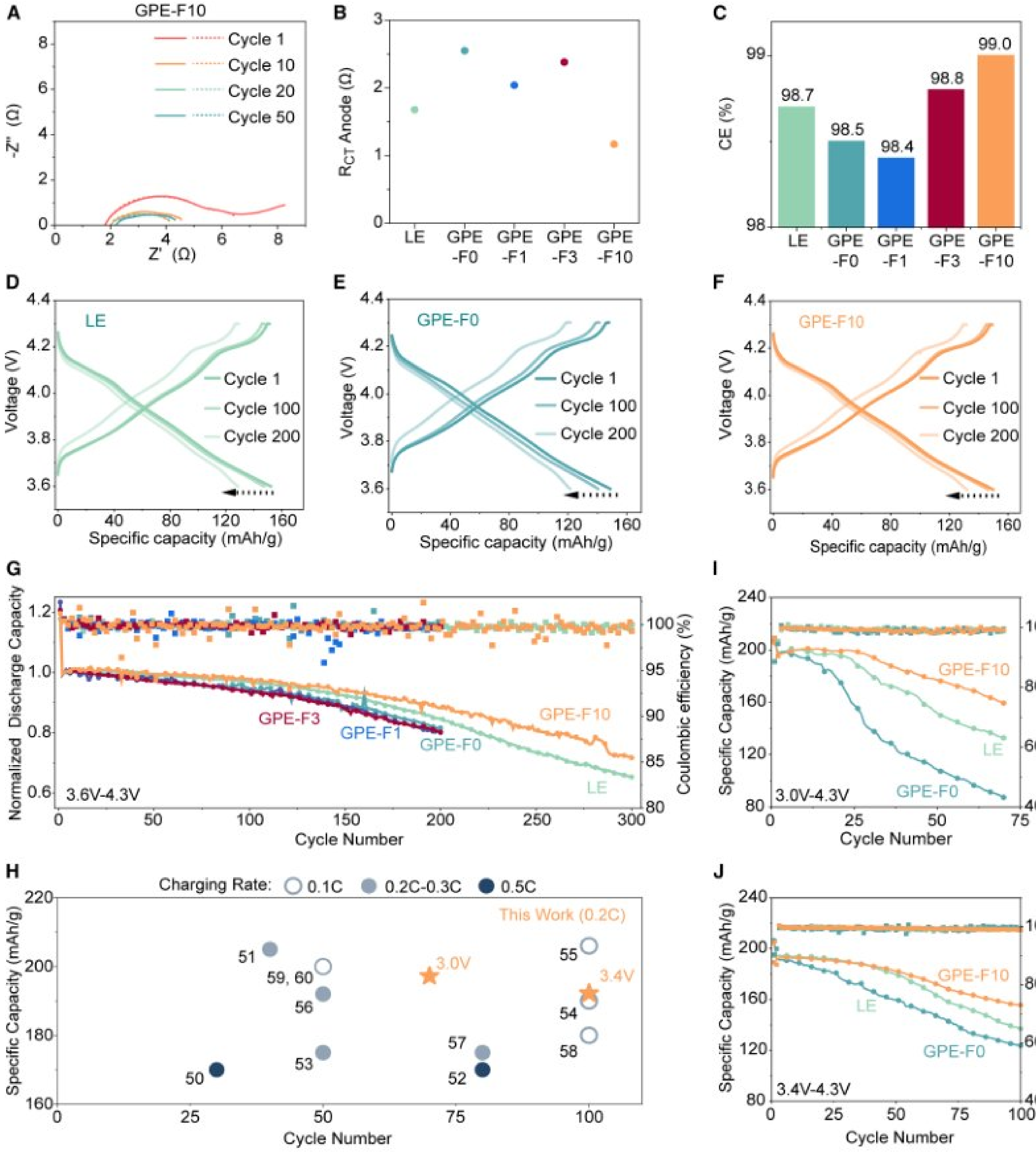

Figure 3. Electrochemical performance of various electrolyte-based anode-free pouch cells

(A) Electrochemical impedance spectra (EIS) of the Cu/GPE-F10/NCA cell after charging in different cycles. Solid lines show the measured data, and dashed lines correspond to the fitted values.

(B) EIS results revealing the evolution of the $R_{ct,\ anode}$ at the 50th cycle in Cu/NCA pouch cells in different electrolytes. The lowest $R_{ct,\ anode}$ is found in GPE-F10 after 50 cycles.

(C) Coulombic efficiency (CE) in Li/Cu half cells using different electrolytes. GPE-F10 shows the highest CE. CE is defined as $Q_{discharge}/Q_{charge}$, where $Q_{discharge}$ is discharge capacity (mAh), and Q_{charge} is charge capacity (mAh).

(D–F) Voltage profiles of Cu/NCA cells at 25°C with (D) LE, (E) GPE-F0, and (F) GPE-F10 electrolytes.

(legend continued on next page)

Please cite this article in press as: Cong et al., Gel electrolyte featuring parasitic salt-phobic network enables anode-free lithium batteries with long cycle life and enhanced thermal stability, Joule (2025), https://doi.org/10.1016/j.joule.2025.102296

Li^+ in GPE-F10.[40,45,46] Meanwhile, CDF curves in Figure S18 show that 2.55 DEC/FEC and 2.49 $DFOB^-/BF_4^-$ coordinate to one Li^+ in GPE-F10. By contrast, more solvents coordinate to one Li^+ found in LE and GPE-F0 (Note S2 and Table S3). Collectively, the results in Figures 2K, 2L, and S15–S17 confirm the formation of an anion-rich solvation structure in GPE-F10.

Electrochemical performance in anode-free cells

To elucidate the effect of anion-rich solvation structure induced by parasitic salt-phobic network on electrochemical performance, the charge transfer resistances (R_{ct}) of Cu/NCA cells are measured by impedance spectroscopy (Figures 3A and S19–S21).[47] At the 50th cycle, GPE-F10 exhibits the lowest $R_{ct,\ anode}$ (1.19 Ω) among five electrolyte compositions, followed by LE (1.68 Ω), GPE-F0 (2.55 Ω), GPE-F1 (2.04 Ω), and GPE-F3 (2.38 Ω) (Figure 3B; Table S4). Such results indicate that the anion-rich solvation structure, induced by the parasitic network in GPE-F10, effectively promotes the formation of an anion-derived SEI and facilitates interfacial charge transfer. Meanwhile, the GPE-F10 also shows a relatively low $R_{ct,\ cathode}$ (1.29 Ω) (Table S4), benefiting the full-cell electrochemical performance.

Additionally, the lowest R_{ct} in GPE-F10 echoes with the Coulombic efficiency (CE) measured in Li/Cu half cells. By using the standard Aurbach method,[48,49] we measured a CE of 98.7% in LE, higher than that of GPE-F0 (98.5%) and GPE-F1 (98.4%), but lower than GPE-F3 (98.8%) and GPE-F10 (99.0%) (Figures 3C and S22). The highest CE observed in GPE-F10 demonstrates its excellent reversibility of lithium plating/stripping. Importantly, such findings support that acrylate polymers alone are not beneficial for fast charge transfer at the lithium/electrolyte interface, but the longer fluorocarbon chains in GPE-F3 and GPE-F10 reverse such disadvantages, making R_{ct} and CE even better than LE. The lowest R_{ct} and highest CE observed in GPE-F10 further translate into remarkable cycling performance in full cells. Cu/NCA single-layer pouch cells were assembled with a size of 1.8 × 1.8 cm, a loading of 4.8 mAh/cm^2 (2.7–4.3 V, with a specific capacity of 210 mAh/g), an electrolyte amount of 6 g/Ah, and an uniaxial external pressure of 0.7 MPa (Figure S23). All cells are charged at 0.2 C and discharged at 0.5 C with a voltage cutoff of 3.6 V after a formation cycle at 0.02 C (1C = 4.8 mA/cm^2).

An operating window of 3.6–4.3 V was first selected, as calculations (Table S5) show that NCA-based anode-free cells deliver 36.3% higher volumetric and 6.3% higher specific energy densities than conventional Li-ion cells (3.0–4.3 V). All electrolytes present stable voltage profiles (Figures 3D–3F and S24). The initial discharge capacity at 0.02 C in 3.6–4.3 V is 175.0, 173.7, 174.1, 173.8, and 173.1 mAh/g for LE, GPE-F0, GPE-F1, GPE-F3, and GPE-F10, respectively. At 0.5 C, these values drop to 150.1, 148.6, 146.7, 146.6, and 146.1 mAh/g, respectively. The slightly higher value in LE at 0.5 C is ascribed to its higher ionic conductivity. As shown in Figure 3G, GPE-F10 leads to a high capacity retention of 88.2% after 200 cycles at 25°C, not only outperforming other gel electrolytes (81.6% for GPE-F0, 80.3% for GPE-F1, and 80.2% for GPE-F3) but also exceeding the benchmark LE (84.6%). Moreover, the Cu/NCA cell with the GPE-F10 electrolyte achieves a capacity retention of 81.8% after 250 cycles and 72.2% after 300 cycles, exceeding the 73.6% retention after 250 cycles and 65.2% after 300 cycles in LE. All cells exhibit highly reproducible cycling performance, as shown in Figure S25, with detailed cycling metrics summarized in Table S6.

In addition, anode-free cells were further tested with lower cutoff voltages to maximize energy density. Within 3.0–4.3 V (Figure 3I), GPE-F10 delivers a high discharge capacity of 197.2 mAh/g at 0.5C and retains 80.1% after 70 cycles, outperforming GPE-F0 (45.4%) and LE (66.2%) (Figure S26; Table S7). Notably, narrowing the window to 3.4–4.3 V results in only a minor capacity loss (~5 mAh/g, 2%–3%) but extends cycle life by over 40%. Under this condition, GPE-F10 achieves 192.2 mAh/g and maintains 80.3% capacity after 100 cycles, markedly surpassing GPE-F0 (64.7%) and LE (70.1%) (Figures 3J and S27; Table S8). The cycling performances under different voltage ranges are summarized in Table S9. As shown in Figure 3H, to the best of our knowledge, this is one of the best cycling performances of anode-free batteries reported so far (Figure S28; Tables S10 and S11).[50–63]

The trend of capacity retention in the five electrolytes above is in accord with R_{ct} and CE results (Figures 3B and 3C), despite GPE-F10's lower ionic conductivity. The lowest R_{ct}, highest CE, and excellent cycling stability collectively highlight the key role of the anion-rich solvation structure, enabled by the parasitic salt-phobic network in the polymer matrix incorporating a long-fluorocarbon-chain fluoroacrylate, in promoting the formation of a high-quality SEI. In addition, GPE-F10 also shows excellent electrochemical stability, as validated by leakage current tests and linear sweep voltammetry (LSV).[64–66] In the leakage current test (Figure S29), GPE-F3 and GPE-F10 deliver lower leakage currents (~0.08 mA/g) than LE, GPE-F0, and GPE-F1 (~0.2 mA/g), indicating suppressed parasitic reactions. Consistently, LSV results reveal that GPE-F10 exhibits the highest oxidation onset (5.39 V), confirming its superior anodic stability (Figure S30). In addition, the key physicochemical and electrochemical properties of the reported gel electrolytes are summarized in Table S12.

SEI composition and lithium deposition morphology

To gain in-depth insight into how the parasitic salt-phobic network formed by interchain interactions of fluorocarbon segments in GPE-F10 affects SEI composition and thus electrochemical performance, cryo-TEM and XPS are used to investigate SEI morphology and composition. In cryo-TEM images, it is found that both GPE-F10 and LE have a thin SEI layer of ~8–10 nm (Figures 4A and S31), while GPE-F0 has a much thicker SEI (>20 nm; Figure S32). This feature effectively reduces

(G) Cycling performance and CE of Cu/NCA cells with different electrolytes from 3.6 to 4.3 V at 25°C. GPE-F10 shows superior performance compared with the other electrolytes.

(I–J) Cycling performance and CE of Cu/NCA pouch cells with LE, GPE-F0, and GPE-F10 between (I) 3.0–4.3 V and (J) 3.4–4.3 V at 25°C.

(H) Comparison of discharge specific capacity vs. cycle number (80% retention as cutoff) with best results in literature. Our results are better than the best previous reports charged at 0.2 C and above. The results are in line with the best reports charged at 0.1 C.

Please cite this article in press as: Cong et al., Gel electrolyte featuring parasitic salt-phobic network enables anode-free lithium batteries with long cycle life and enhanced thermal stability, Joule (2025), https://doi.org/10.1016/j.joule.2025.102296

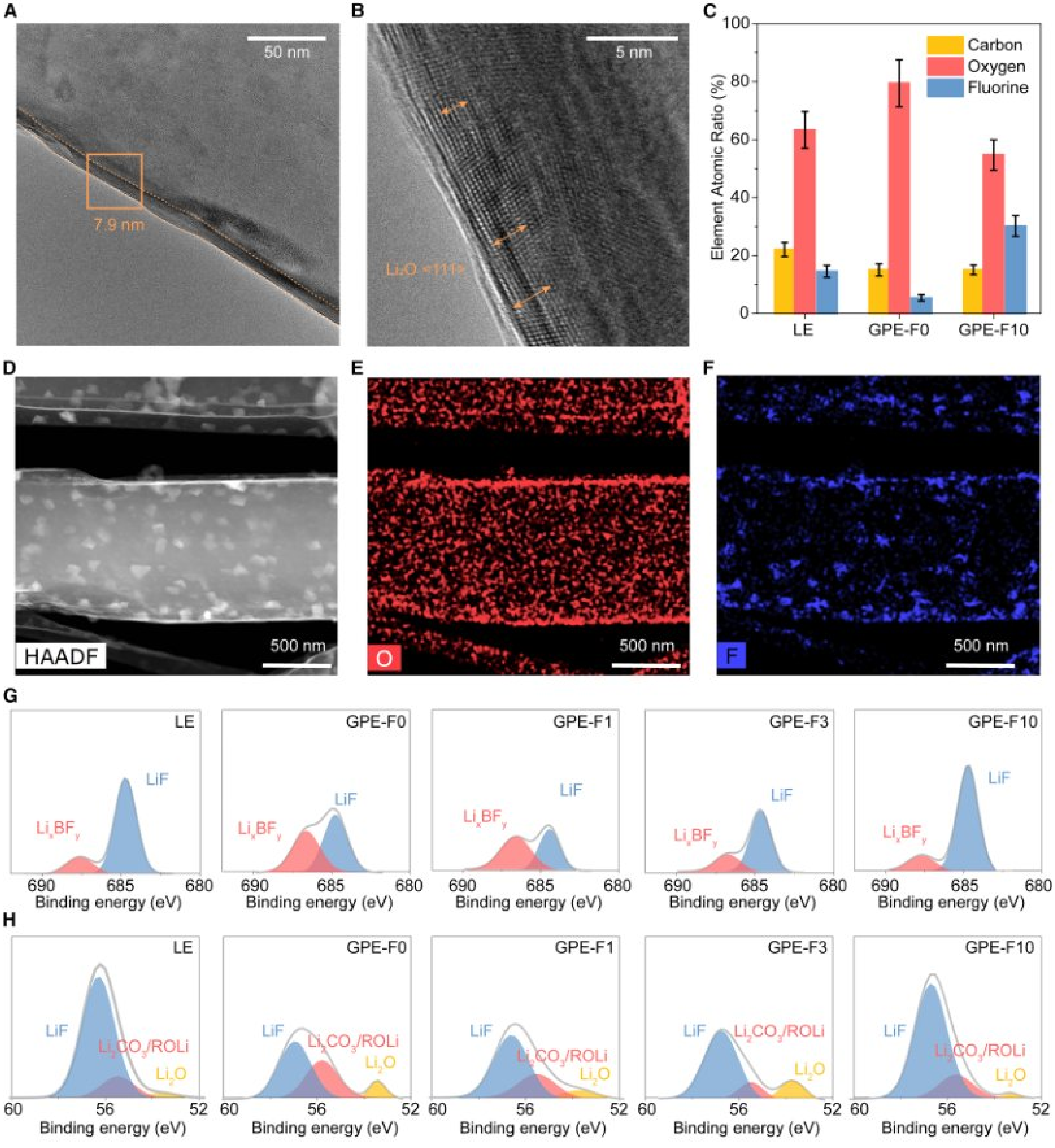

Figure 4. SEI characterizations

(A) A cryo-TEM image of the SEI layer on lithium metal deposited from GPE-F10 electrolyte, showing a thin SEI (~ 8 nm). Magnification is 600,000, and voltage is 200 kV.

(B) Atomic-resolution image of the orange region outlined in (A), showing the structure of the SEI layer. The lattice spacing of small crystalline grains matches Li_2O. Magnification is 5,000,000, and voltage is 200 kV.

(C) Atomic percentage of carbon, oxygen, and fluorine elements in SEI on lithium metal in cells with LE, GPE-F0, and GPE-F10. The highest fluorine percentage is observed in GPE-F10. The error bars indicated standard deviation.

(D–F) High-angle annular dark-field (HAADF)-STEM and corresponding (E) oxygen, and (F) fluorine EDS elemental mapping of as-deposited lithium metal. Magnification is 57,000, and voltage is 200 kV.

(G and H) XPS spectra of F *1s* (G) and Li *1s* (H) of the top surface of lithium deposition in cells with different electrolytes at the end of charging in the 3rd cycle. Compared with other gel electrolytes, GPE-F10 exhibits a higher LiF percentage in SEI composition.

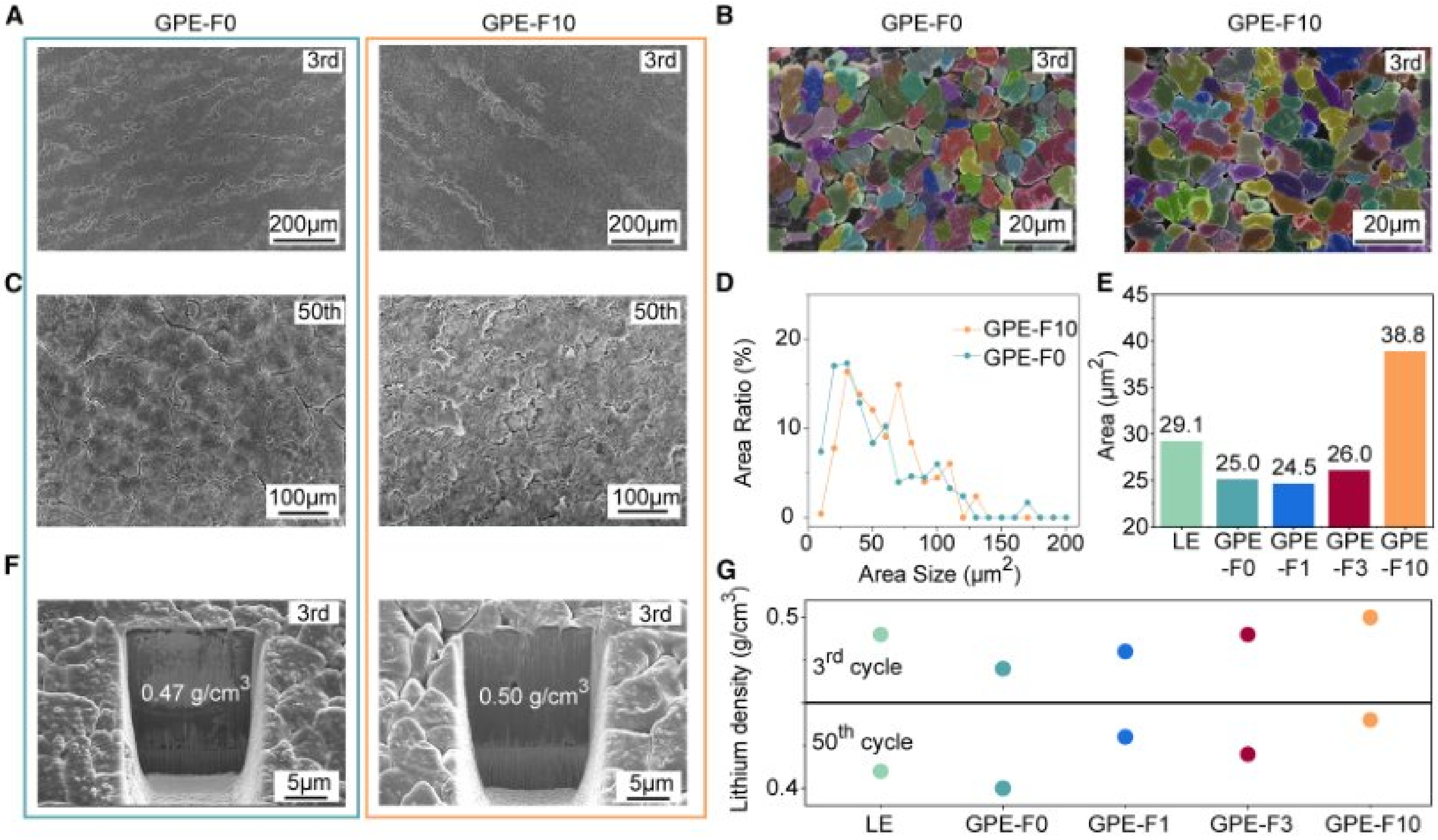

Figure 5. Lithium metal deposition characterization

(A and B) SEM images of lithium morphology deposited on Cu for GPE-F0 and GPE-F10 at (A) mesoscale and (B) microscale scale. Images were taken at the end of charging in the 3rd cycle, showing a more uniform deposition in GPE-F10. The voltage is 10 kV. The magnification is 120 for (A) and 1,200 for (B).

(C) SEM images of lithium morphology deposited on Cu for GPE-F0 and GPE-F10. Images were taken at the end of charging in the 50th cycle, exhibiting a more compact deposition in GPE-F10. The voltage is 10 kV, and the magnification is 300.

(D) Lithium metal domain size distribution from cells with GPE-F0 and GPE-F10 electrolytes (3rd cycle).

(E) GPE-F10 shows the largest domain size compared with other electrolytes at the end of the 3rd cycle.

(F) Cross-sectional view of lithium deposition from FIB-SEM images (3rd cycle). The voltage is 5 kV, and the magnification is 3,500.

(G) GPE-F10 shows the highest density of as-deposited lithium metal compared with other electrolytes after the 3rd charging and the 50th charging.

lithium consumption caused by SEI formation during each cycle, thus enhancing the CE. Furthermore, high-resolution imaging indicates that the thin layer on the surface is crystalline Li_2O (Figure 4B), as the lattice spacing of 2.68 Å matches that of the (111) plane of Li_2O.[67] The electron diffraction (ED) image also shows clear Friedel pairs of the (110) plane of lithium metal and the (111) plane of polycrystalline rings of Li_2O, with the absence of LiF signals (Figure 4D). However, numerous fluorine-rich surface domains, with sizes ranging from 50 to 100 nm, are identified in the energy-dispersive spectroscopy (EDS) mapping (Figures 4D and 4F). Such a difference can be explained as that the fluorine-rich domains are amorphous.[68] Importantly, the EDS analysis shows that the lithium metal surface in a cell with GPE-F10 electrolyte has the highest fluorine portion (30.2%), followed by LE (14.5%) and GPE-F0 (5.4%) (Figure 4C).

Additionally, the XPS depth profile reveals the difference in SEI composition among the five electrolytes. In the F *1s* spectra (Figures 4G and S33), the LE and GPE-F10 show a dominant LiF peak at 684.7 eV[69] with atomic percentages of 81.5% and 83.8%, respectively, on the SEI surface, while GPE-F0, GPE-F1, and GPE-F3 show a significant portion of Li_xBF_y at 687.2 eV[70] in the range of 21%–55%, supporting that anion-rich solvation promotes a LiF-rich SEI, which is beneficial for long-term battery cycling. The same trend of a more LiF-rich SEI in LE and GPE-F10 is found in Li *1s* spectra (Figures 4H and S34), consistent with the F mapping results in Figure 4C, further corroborating the anion-derived SEI composition. In addition, the typical peaks of C *1s* spectra assigned to C−C, C−O, and C=O mainly come from ROLi, $ROCO_2Li$, and Li_2CO_3, respectively[70] (Figure S35). Meanwhile, the reduction of $LiBF_4$ and LiDFOB forms a robust SEI with high inorganic species to support long cycling (Figure S36).[55] Therefore, the lower intensity of the C *1s* signal observed in GPE-F10 compared with other electrolytes suggests a more effective suppression of solvent decomposition, attributed to the LiF-dominated SEI facilitated by the anion-rich solvation structure.

The fluorine-rich SEI in GPE-F10 also better regulates interfacial charge transfer and results in smoother lithium deposition. As-deposited lithium metal in GPE-F10 shows less defective surface morphology compared with other electrolytes at both mesoscale (Figures 5A and S37) and microscale (Figures 5B and S38). For example, at the end of charging in the 3rd cycle, the average domain size of lithium metal is 38.8 μm^2 in the

Please cite this article in press as: Cong et al., Gel electrolyte featuring parasitic salt-phobic network enables anode-free lithium batteries with long cycle life and enhanced thermal stability, Joule (2025), https://doi.org/10.1016/j.joule.2025.102296

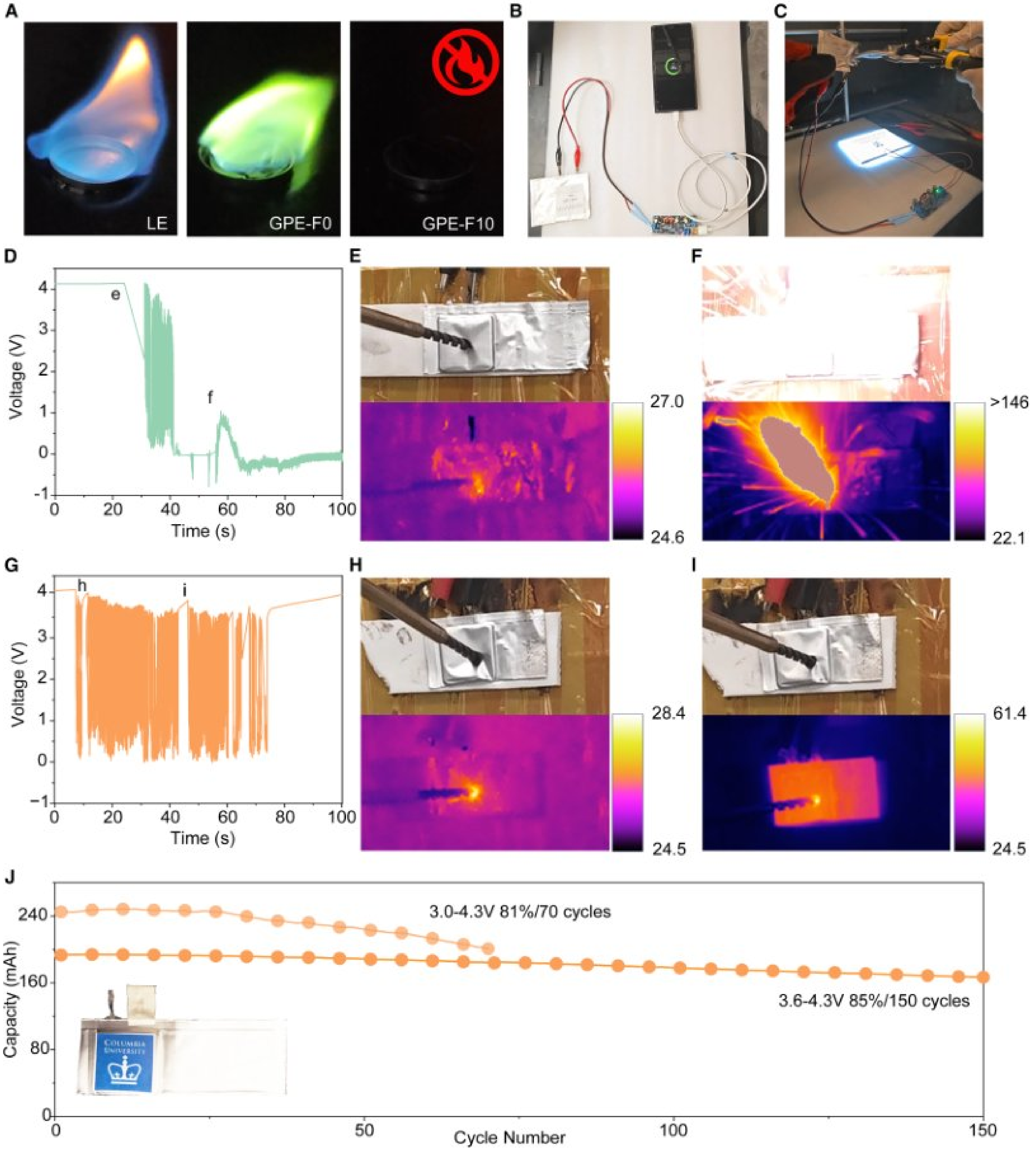

Figure 6. Cu/NCA multi-layer pouch cells' performance under abuse conditions

The nominal capacities of all cells are 240 mAh in 3.0–4.3 V.

(A) Combustion test for LE, GPE-F0 and GPE-F10, and GPE-F10 shows an enhanced thermal stability.

(B) Images of a smartphone powered by a Cu/NCA cell using GPE-F10.

(C) Images of an illuminated panel powered by a Cu/NCA cell using GPE-F10 electrolyte after cutting.

(D–F) Voltage monitoring of LE-based anode-free pouch cell during drilling test. Illustration of snapshots of temperature changes before (E) and after (F) the drilling test monitored by infrared thermography. LE shows poor thermal stability in the drilling test.

(legend continued on next page)

Please cite this article in press as: Cong et al., Gel electrolyte featuring parasitic salt-phobic network enables anode-free lithium batteries with long cycle life and enhanced thermal stability, Joule (2025), https://doi.org/10.1016/j.joule.2025.102296

GPE-F10 electrolyte (Figures 5D, 5E, and S39), which is substantially higher than other electrolytes (e.g., 29.1 μm^2 for LE and 25.0 μm^2 for GPE-F0). Furthermore, GPE-F10 cells exhibit more compact lithium deposition and larger domain size than other electrolytes after 50 cycles (Figures 5C and S40).

In addition to larger domains and fewer defects, GPE-F10 also leads to denser deposition, as revealed by focused ion beam-SEM (FIB-SEM) cross-sectional images. Specifically, after charging in the 3rd and the 50th cycles, the densities of as-deposited lithium are 0.50 and 0.44 g/cm^3 in GPE-F10, respectively, which are higher than 0.49/0.41, 0.47/0.40, 0.48/0.43, and 0.49/0.42 g/cm^3 for LE, GPE-F0, GPE-F1, and GPE-F3, respectively (Figures 5F, 5G, S41, and S42). It is worth noting that such a larger domain size and lithium metal density found in GPE-F10 effectively alleviates the parasitic reactions between electrolyte and lithium, which are crucial to cycling performance as discussed in Figures 3G, 3I, and 3J. The fading in discharge capacity is mainly attributed to the accumulation of dead lithium and the thickening SEI, as evidenced by the FIB (Figures 5G and S42) results after 50 cycles. Post-mortem analysis of cells (Figures S43–S45) after long-term cycling (3.0–4.3 V, 0.2C/0.5C) shows that cathodes remain dense and chemically stable, while anodes exhibit loose, defective lithium deposits. These results confirm that the anion-rich solvation strategy forms a robust anion-derived SEI, stabilizing lithium plating/stripping, suppressing dendrites, and mitigating anode-driven capacity fading. Moreover, the findings of domain size and density of lithium metal above correlate well with the LiF content in SEI (Figure S46), strongly supporting our design that an anion-rich solvation structure induced by a parasitic salt-phobic network successfully promotes a LiF-rich SEI, thus better charge transfer, stable lithium metal morphology, and superior cycling performance in pouch cells.

Safety characterization and cycling performance in multi-layer pouch cells

GPE-F10 exhibits excellent thermal stability. First, the differential scanning calorimetry (DSC) shows that GPE-F10 generates ~30% less heat than GPE-F0, F1, and F3 (Figure S47A), which shows enhanced thermal stability. The thermogravimetric analysis (TGA) also shows slightly slower mass loss in GPE-F10 than in other gel electrolytes (Figure S47B). Such results validate the advantage of GPE-F10 in terms of thermal stability. Besides, when ignited by a butane torch, LE, GPE-F0, and GPE-F1 electrolytes caught fire easily, but both GPE-F3 and GPE-F10 could not be ignited after sustained exposure to the fire source (Figures 6A and S48). Such a difference is attributed to the higher concentration of fluorine radicals (F·) generated from GPE-F3 and GPE-F10 during heating, which combine with H· radicals from DEC/FEC,[18,71] the key component for electrolyte combustion, and reduce the flammability of GPE-F3 and GPE-F10.

Impressively, the 240 mAh Cu/NCA multi-layer pouch cell with the GPE-F10 electrolyte can pass the harsh drilling test at the fully charged state (Video S1). During drilling, the central temperature only rises to ~60°C (Figures 6H and 6I), and the cell voltage recovers after the drill was removed (Figure 6G), highlighting the excellent safety of GPE-F10-based pouch cells. By contrast, a fully charged 240 mAh Cu/NCA cell with LE exploded during drilling with a central temperature >146°C (Figures 6E and 6F; Video S2), and the voltage dropped to 0 V after drilling (Figure 6D). Apart from drilling, the 240 mAh Cu/NCA multi-layer pouch cell with GPE-F10 electrolyte can continuously provide steady power output under harsh conditions, including severe deformation and cutting (Figures 6B, 6C, and S49).

Moreover, the GPE-F10 electrolyte shows impressive cycling performance in multi-layer Cu/NCA pouch cells (Figure 6J). The NCA loading is 3.1 mAh/cm^2, and the electrolyte content is only 2.8 g/Ah. In the voltage range of 3.6–4.3 V, the initial discharge capacity reaches 152.6 mAh/g (192.1 mAh) at 0.5 C, and the capacity remains 84.8% after 150 cycles. Additionally, within the voltage range of 3.0–4.3 V, a stacking Cu/NCA pouch cell delivers a discharge capacity of 196.5 mAh/g (245.6 mAh) and a retention of 81.2% after 70 cycles at 0.5C. Such cycling performance is highly reproducible in pouch cells (Figures S50 and S51). The safety and cycling results in the large pouch cells above mark the remarkable advantages of the parasitic salt-phobic network design strategy toward high-performance and safe anode-free LMBs.

DISCUSSION

In summary, we developed a fluoroacrylate-based gel polymer electrolyte featuring a parasitic salt-phobic network that simultaneously achieves excellent cycle life and enhanced thermal stability for anode-free Li-metal batteries. This unique secondary architecture formed by aggregated fluoroacrylate offers distinct advantages over conventional LHCEs. First, the salt-phobic network precisely regulates Li$^+$ solvation to form a high-quality, anion-rich SEI, unlike the limited solvation control in LHCEs. Second, the polymer phase provides markedly improved thermal stability. Last, the low fluorinated-acrylate content reduces both cost and electrolyte density, benefiting cell-level energy density.

Using this design philosophy, GPE-F10 exhibits a smoother lithium deposition morphology and higher density than the corresponding liquid and other polymer gel electrolytes. With GPE-F10, 240 mAh Cu/NCA anode-free pouch cells deliver an initial capacity of 196.5 mAh/g and retain 81.2% after 70 cycles at 3.0–4.3 V. Narrowing the voltage window to 3.4–4.3 V and 3.6–4.3 V further improves capacity retention to 80.3% over 100 cycles and 87.2% over 200 cycles, respectively. Notably, such pouch cells with GPE-F10 pass the drilling test without thermal runaway. Overall, our parasitic network design establishes a foundation for high-performance anode-free LMBs in a safe manner. Such a design concept can be extended to other alkali metal batteries for optimizing SEI compositions. Future work will focus on refining the fluoropolymer network to precisely control domain size, composition, and dynamics. By tuning the polymer backbone and salt-polymer interactions, the nanoscale

(G–I) (G) Voltage monitoring of GPE-F10-based Cu/NCA pouch cell during the drilling test. Illustration of snapshots of temperature changes (H) before and (I) after the drilling test monitored by infrared thermography. GPE-F10 exhibits no thermal runaway in the drilling test.

(J) Cycling performance of the Cu/NCA pouch cells using the GPE-F10 at 0.2 C charge and 0.5 C discharge between 3.0–4.3 V and 3.6–4.3 V after 0.02 C formation with a lean electrolyte 2.8 g/Ah (25°C), showing attractive performance.

Please cite this article in press as: Cong et al., Gel electrolyte featuring parasitic salt-phobic network enables anode-free lithium batteries with long cycle life and enhanced thermal stability, Joule (2025), https://doi.org/10.1016/j.joule.2025.102296

solvation environment can be optimized to balance ion transport and interfacial stability. Extending this parasitic salt-phobic network strategy across diverse polymers, salts, and solvents could provide a general design principle for next-generation gel polymer electrolytes with improved safety and performance.

METHODS

Materials

The NCA cathode electrode (94.5 wt % NCA) with a total areal capacity of 4.8 mAh/cm^2 was acquired from Samsung SDI R&D America. 240 mAh anode-free dry cells were purchased from Canrd Technology Co. Ltd. Lithium tetrafluoroborate ($LiBF_4$, 99%), lithium difluoro(oxalato)borate (LiDFOB, 99%), diethyl carbonate (DEC, 99%), and fluoroethylene carbonate (FEC, 99%) were purchased from Gotion. TMPTMA (99%), 2,2,2-trifluoroethyl acrylate (TFEA, 99%), 2,2,3,4,4,4-hexafluorobutyl acrylate (HFBA, 98%), 3,3,4,4,5,5,6,6,7,7,8,8,9,9,10,10,11,11,12,12,12-HFDA (96%), and azobisisobutyronitrile (AIBN, 98%) were purchased from Sigma-Aldrich. Other battery materials, such as 2032-type coin-cell cases, springs, and spacers, were all purchased from Hunan Li-Fun Technology. All electrolytes tested in this study were prepared inside an Ar-filled glovebox with $O_2 < 0.1$ ppm and $H_2O < 0.1$ ppm.

Liquid and polymer gel electrolyte preparation

The dual-salt liquid electrolyte is prepared by dissolving 1.0 M LiDFOB and 0.4 M $LiBF_4$ in a mixture of DEC/FEC (2:1 by volume). To prepare the GPE-F0, 5 wt % TMPTMA monomer and 0.15 wt % AIBN initiator were dissolved in the prepared dual-salt solution (95 wt %) as the precursor. The precursor solution was added to the anode-free pouch cells and heated at 55°C for 12 h under a pressure of 0.7 MPa to ensure a full polymerization of the monomers. Similarly, to prepare the GPE-FX (X = 1, 3, and 10), 2.5 wt % fluoroacrylate monomer, 2.5 wt % TMPTMA monomer, and 0.15 wt % AIBN initiator were dissolved in dual-salt solution (95 wt %) as a precursor. Then, the precursor solution was added to the anode-free pouch cells and heated at 55°C for 12 h under a pressure of 0.7 MPa.

Material characterizations

All SEM images were characterized on a Zeiss Sigma VP SEM at 8.0 kV to elucidate the morphological evolution of the Li-metal anodes. The chemical composition of the SEI was analyzed by the PHI Versaprobe II XPS with a monochromatic Al Kα X-ray excitation source (1,486.6 eV). The samples were loaded in an airtight vessel in an Ar glovebox and transferred to XPS without any air exposure. The Li-metal anodes used for XPS depth-profiling analysis were collected from the Cu/NCA pouch cells at the end of charging in the 3rd cycle. For the XPS characterization, all the collected Li-metal anodes were washed three times with DEC to remove any electrolyte residues, followed by drying at 50°C for 10 min. Electrochemical impedance spectroscopy tests on the Cu/NCA anode-free pouch cells in different electrolytes were carried out on a Bio-Logic SAS VMP3 and performed at an amplitude of 10 mV in the frequency range of 1 MHz to 0.1 Hz.

Cryo-TEM characterization

The Li samples for cryo-TEM characterization were prepared by electroplating Li onto bare Cu cryo-TEM grids at 0.48 mA/cm^2 for 30 min using the corresponding electrolytes. The resultant Li samples on Cu grids were washed with DEC, dried at 50°C for 10 min, then used for the cryo-TEM analysis. A dual spherical aberration-corrected FEI Titan2 G2 60–300 STEM was used to collect the TEM and STEM images by operating at an accelerating voltage of 200 kV. A Gatan GIF Quantum ERS 966 system, with settings adjusted to an energy dispersion of 0.05 eV per channel, an exposure time of 0.1 s, and a maintained 10 nm pixel size, was utilized to collect the electron energy loss spectroscopy (EELS) spectra. Energy-dispersive X-ray spectroscopy mapping images were acquired using Bruker Super-X quad X-ray detectors with a beam current of 0.1 nA in 5 min.

Pouch cell assembly

The pouch cells in this study were fabricated inside a glovebox using a single-sided coated NCA electrode (18 × 18 mm), 1 piece of bare Cu (35 × 25 mm), 1 piece of separator (25 × 35 mm), and 1 piece of Al (20 × 30 mm). Each single pouch cell used 95 μl (6 g/Ah) of corresponding electrolyte and was heated at 55°C for 12 h. For the anode-free multi-layer pouch cells (240 mAh) using GPE-F10, the preparation is the same as the aforementioned process, except for the electrolyte amount (2.8 g/Ah), and 0.67 g of electrolyte was added to the 240 mAh pouch cells.

Electrochemical testing

All electrochemical evaluations of the pouch cells and coin cells were conducted using Landt battery testers. Cu/NCA anode-free cells were assembled with a single-sided coated NCA electrode and the corresponding electrolyte under a pressure of 0.7 MPa. The pouch cells were tested under galvanostatic charging and discharging conditions. After one formation cycle with both charging and discharging at 0.02C, the pouch cells were then charged at 0.2C and discharged at 0.5C for cycling within the voltage window of 3.6–4.3, 3.4–4.3, or 3.0–4.3 V. For CE evaluation, all Li/Cu coin cells were assembled using 80 μl of the corresponding electrolyte and tested at constant current and constant voltage charging protocol.

Computation details

DFT calculations were performed for the set of ions and ion-molecular complexes optimized in the gas phase using the M06-2X/6-311++G(d, p) level of theory using the Gaussian code. For classical MD, the optimized potentials for liquid simulations – all atom (OPLS-AA) force field was utilized to adjust most of the intra- and interatomic potential parameters. To evaluate the interaction strength between Li ions and various molecular species, we performed first-principles calculations using the Vienna Ab initio Simulation Package (VASP). The binding energies between Li^+ and the selected molecules were computed to assess their relative affinities. To account for solvation effects, all calculations were carried out under implicit solvent conditions using the VASPsol module, which simulates the presence of a dielectric continuum representing the solvent environment.

The electronic self-consistent field (SCF) convergence criterion was set to 1 × 10^{-5} eV, and the structures were relaxed until the residual forces on each atom were below 0.02 eV/Å, ensuring reliable and well-converged results. More details can be found in Note S2.

RESOURCE AVAILABILITY

Lead contact

Requests for further information and resources should be directed to and will be fulfilled by the lead contact, Yuan Yang (yy2664@columbia.edu).

Materials availability

This study did not generate new, unique reagents.

Data and code availability

- All data reported in this paper will be shared by the lead contact upon request.
- This paper does not report original code.
- Any additional information required to reanalyze the data reported in this paper is available from the lead contact upon request.

ACKNOWLEDGMENTS

Yuan Yang acknowledges support from the Samsung SDI R&D Center in Suwon and America.

AUTHOR CONTRIBUTIONS

Supervision, YuanYang; conceptualization, S.C., Z.Y., and YuanYang; methodology, S.C., Z.Y.; investigation, S.C., Z.Y., X.W., H.C., S.Y., Z.Y., YuchenYang, T.W., S.Z., M.N.N., Y.G., Y.M., Y.L., H.W., S.W.L., Y.K., and Yuan Yang; writing – reviewing & editing, S.C., Z.Y., and YuanYang All authors have read and agreed to the published version of the manuscript.

DECLARATION OF INTERESTS

We have one patent related to this work that is being filed.

DECLARATION OF GENERATIVE AI AND AI-ASSISTED TECHNOLOGIES IN THE WRITING PROCESS

During the preparation of this work, the authors used ChatGPT in order to polish the language. After using this tool or service, the authors reviewed and edited the content as needed and take full responsibility for the content of the publication.

SUPPLEMENTAL INFORMATION

Supplemental information can be found online at https://doi.org/10.1016/j.joule.2025.102296.

Received: June 9, 2025
Revised: November 6, 2025
Accepted: December 12, 2025

REFERENCES

1. Kim, S.C., Wang, J., Xu, R., Zhang, P., Chen, Y., Huang, Z., Yang, Y., Yu, Z., Oyakhire, S.T., Zhang, W., et al. (2023). High-entropy electrolytes for practical lithium metal batteries. Nat. Energy *8*, 814–826. https://doi.org/10.1038/s41560-023-01280-1.
2. Xiao, J., Li, Q., Bi, Y., Cai, M., Dunn, B., Glossmann, T., Liu, J., Osaka, T., Sugiura, R., Wu, B., et al. (2020). Understanding and applying coulombic efficiency in lithium metal batteries. Nat. Energy *5*, 561–568. https://doi.org/10.1038/s41560-020-0648-z.
3. Yin, X., Li, B., Liu, H., Wen, B., Liu, J., Bai, M., Zhang, Y., Zhao, Y., Cui, X., Su, Y., et al. (2025). Solvent-derived organic-rich SEI enables capacity enhancement for low-temperature lithium metal batteries. Joule *9*, 101823. https://doi.org/10.1016/j.joule.2025.101823.
4. Liu, Y., Tao, X., Wang, Y., Jiang, C., Ma, C., Sheng, O., Lu, G., and Lou, X.W.D. (2022). Self-assembled monolayers direct a LiF-rich interphase toward long-life lithium metal batteries. Science *375*, 739–745. https://doi.org/10.1126/science.abn1818.
5. Chen, Y., Li, M., Jie, Y., Liu, Y., Zhang, Z., Yu, P., Li, W., Liu, Y., Li, X., Lei, Z., et al. (2025). Dynamic evolution of cathode-electrolyte interphase in lithium metal batteries with ether electrolytes. Joule *9*, 101885. https://doi.org/10.1016/j.joule.2025.101885.
6. Wang, Z., Xia, J., Ji, X., Liu, Y., Zhang, J., He, X., Zhang, W., Wan, H., and Wang, C. (2024). Lithium anode interlayer design for all-solid-state lithium-metal batteries. Nat. Energy *9*, 251–262. https://doi.org/10.1038/s41560-023-01426-1.
7. Fang, M., Yue, X., Dong, Y., Chen, Y., and Liang, Z. (2024). A temperature-dependent solvating electrolyte for wide temperature and fast-charging lithium metal batteries. Joule *8*, 91–103. https://doi.org/10.1016/j.joule.2023.12.012.
8. Sandoval, S.E., Haslam, C.G., Vishnugopi, B.S., Liao, D.W., Yoon, J.S., Park, S.H., Wang, Y., Mitlin, D., Hatzell, K.B., Siegel, D.J., et al. (2025). Electro-chemo-mechanics of anode-free solid-state batteries. Nat. Mater. *24*, 673–681. https://doi.org/10.1038/s41563-024-02055-z.
9. Sandoval, S.E., Lewis, J.A., Vishnugopi, B.S., Nelson, D.L., Schneider, M.M., Cortes, F.J.Q., Matthews, C.M., Watt, J., Tian, M., Shevchenko, P., et al. (2023). Structural and electrochemical evolution of alloy interfacial layers in anode-free solid-state batteries. Joule *7*, 2054–2073. https://doi.org/10.1016/j.joule.2023.07.022.
10. Weber, R., Genovese, M., Louli, A.J., Hames, S., Martin, C., Hill, I.G., and Dahn, J.R. (2019). Long cycle life and dendrite-free lithium morphology in anode-free lithium pouch cells enabled by a dual-salt liquid electrolyte. Nat. Energy *4*, 683–689. https://doi.org/10.1038/s41560-019-0428-9.
11. Qiao, Y., Yang, H., Chang, Z., Deng, H., Li, X., and Zhou, H. (2021). A high-energy-density and long-life initial-anode-free lithium battery enabled by a Li_2O sacrificial agent. Nat. Energy *6*, 653–662. https://doi.org/10.1038/s41560-021-00839-0.
12. Nanda, S., Bhargav, A., and Manthiram, A. (2020). Anode-free, lean-electrolyte lithium-sulfur batteries enabled by tellurium-stabilized lithium deposition. Joule *4*, 1121–1135. https://doi.org/10.1016/j.joule.2020.03.020.
13. Louli, A.J., Eldesoky, A., Weber, R., Genovese, M., Coon, M., deGooyer, J., Deng, Z., White, R.T., Lee, J., Rodgers, T., et al. (2020). Diagnosing and correcting anode-free cell failure via electrolyte and morphological analysis. Nat. Energy *5*, 693–702. https://doi.org/10.1038/s41560-020-0668-8.
14. Su, L., Charalambous, H., Cui, Z., and Manthiram, A. (2022). High-efficiency, anode-free lithium–metal batteries with a close-packed homogeneous lithium morphology. Energy Environ. Sci. *15*, 843–854. https://doi.org/10.1039/d1ee03103a.
15. Liang, P., Sun, H., Huang, C.L., Zhu, G., Tai, H.C., Li, J., Wang, F., Wang, Y., Huang, C.J., Jiang, S.K., et al. (2022). A Nonflammable High-Voltage 4.7 V Anode-Free Lithium Battery. Adv. Mater. *34*, e2207361. https://doi.org/10.1002/adma.202207361.
16. Molaiyan, P., Abdollahifar, M., Boz, B., Beutl, A., Krammer, M., Zhang, N., Tron, A., Romio, M., Ricci, M., Adelung, R., et al. (2024). Optimizing Current Collector Interfaces for Efficient "Anode-Free" Lithium Metal Batteries. Adv. Funct. Mater. *34*, 2311301. https://doi.org/10.1002/adfm.202311301.
17. Masias, A., Felten, N., Garcia-Mendez, R., Wolfenstine, J., and Sakamoto, J. (2019). Elastic, plastic, and creep mechanical properties of lithium metal. J. Mater. Sci. *54*, 2585–2600. https://doi.org/10.1007/s10853-018-2971-3.
18. Hu, A., Chen, W., Li, F., He, M., Chen, D., Li, Y., Zhu, J., Yan, Y., Long, J., Hu, Y., et al. (2023). Nonflammable polyfluorides-anchored quasi-solid

electrolytes for ultra-safe anode-free lithium pouch cells without thermal runaway. Adv. Mater. *35*, e2304762. https://doi.org/10.1002/adma.202304762.

19. Dong, L., Zhong, S., Zhang, S., Yuan, B., Liu, J., Xie, H., Zhang, C., Liu, Y., Yang, C., Han, J., et al. (2023). Toward practical anode-free lithium pouch batteries. Energy Environ. Sci. *16*, 5605–5632. https://doi.org/10.1039/d3ee01599h.
20. Huo, S., Wang, L., Su, B., Xue, W., Wang, Y., Zhang, H., Li, M., Qiu, J., Xu, H., and He, X. (2024). Anode-Free Li Metal Batteries: Feasibility Analysis and Practical Strategy. Adv. Mater. *36*, e2411757. https://doi.org/10.1002/adma.202411757.
21. Yi, R., Xu, K., Zhao, W., Ren, Z., Dong, Q., Shao, H., Shen, Y., and Chen, L. (2025). Coordination Topology Design in Anion-Rich Solvated Electrolytes for High-Voltage Lithium Metal Batteries. Angew. Chem. Int. Ed. Engl. *64*, e202423439. https://doi.org/10.1002/anie.202423439.
22. Ding, F., Li, Y., Zhang, G., Wang, H., Liu, B., Liu, C., Jiang, L., Sui, X., and Wang, Z. (2024). High-safety electrolytes with an anion-rich solvation structure tuned by difluorinated cations for high-voltage lithium metal batteries. Adv. Mater. *36*, e2400177. https://doi.org/10.1002/adma.202400177.
23. Zhou, P., Ou, Y., Feng, Q., Xia, Y., Zhou, H., Hou, W.h., Song, X., Lu, Y., Yan, S., and Zhang, W. (2025). Tuning the Nucleophilicity of Anion in Lithium Salt to Enable an Anion-Rich Solvation Sheath for Stable Lithium Metal Batteries. Adv. Funct. Mater *35*, 2416800. https://doi.org/10.1002/adfm.202416800.
24. Liu, R., Xu, Y.S., Zhou, R., Tan, S.J., Li, Y.N., Jiang, S.J., Xin, S., Guo, Y.G., and Cao, F.F. (2025). Localized High-Concentration Electrolyte for All-Carbon Rechargeable Dual-Ion Batteries with Durable Interfacial Chemistry. Angew. Chem. Int. Ed. Engl. *64*, e202416610. https://doi.org/10.1002/anie.202416610.
25. Wang, C., Wan, K., Liu, P., Zeng, C., Wang, S., Huang, Y., Zhang, Y., Xiao, H., Shu, C., and Liang, Z. (2025). Localized High-Concentration Electrolytes With Semi-Solvated Hexafluoroisopropyl Methyl Ether Diluent for Wide-Temperature-Range Lithium Metal Batteries. Angew. Chem. Int. Ed. Engl. *64*, e202506083. https://doi.org/10.1002/anie.202506083.
26. Wu, Q., and Qi, Y. (2025). Revealing heterogeneous electric double layer (EDL) structures of localized high-concentration electrolytes (LHCEs) and their impact on solid–electrolyte interphase (SEI) formation in lithium batteries. Energy Environ. Sci. *18*, 3036–3046. https://doi.org/10.1039/d5ee00206k.
27. Li, P., Zhang, Z., Zhao, Z., Zhang, X., Zhang, H., and Li, G. (2024). Localized medium concentration electrolyte with fast kinetics for lithium metal batteries. Angew. Chem. Int. Ed. Engl. *63*, e202319090. https://doi.org/10.1002/anie.202319090.
28. Huang, Y., Li, R., Weng, S., Zhang, H., Zhu, C., Lu, D., Sun, C., Huang, X., Deng, T., Fan, L., et al. (2022). Eco-friendly electrolytes via a robust bond design for high-energy Li metal batteries. Energy Environ. Sci. *15*, 4349–4361. https://doi.org/10.1039/d2ee01756c.
29. Xia, S., Zhang, X., Jiang, Z., Wu, X., Yuwono, J.A., Li, C., Wang, C., Liang, G., Li, M., Zhang, F., et al. (2025). Ultrathin Polymer Electrolyte With Fast Ion Transport and Stable Interface for Practical Solid-state Lithium Metal Batteries. Adv. Mater. *37*, e2510376. https://doi.org/10.1002/adma.202510376.
30. Feng, J., Wang, J., Gu, Q., Li, P., Xu, H., Deng, Y., and Gao, P. (2025). 1 μm-Thick Robust Gel Polymer Electrolyte with Excellent Interfacial Stability for High-Performance Li Metal Batteries. Adv. Funct. Mater. *35*, 2412287. https://doi.org/10.1002/adfm.202412287.
31. Chikkatti, B.S., Sajjan, A.M., Kalahal, P.B., Banapurmath, N.R., Khan, T.M.Y., Khadar, S.D.A., Shamsudeen, S.M., and Raju, A.B. (2022). A novel poly (vinyl alcohol)–tetraethylorthosilicate hybrid gel electrolyte for lead storage battery. Gels *8*, 791. https://doi.org/10.3390/gels8120791.
32. Chikkatti, B.S., Sajjan, A.M., Banapurmath, N.R., Bhutto, J.K., Verma, R., and Yunus Khan, T.M. (2023). Fabrication of Flexible Films for Supercapacitors Using halloysite nano-clay Incorporated Poly(lactic acid). Polymers *15*, 4587. https://doi.org/10.3390/polym15234587.
33. Chikkatti, B.S., Sajjan, A.M., Kalahal, P.B., Banapurmath, N.R., and Ayachit, N.H. (2023). Fabrication and assessment of poly (lactic acid)-poly (4-styrene sulfonate) flexible membranes as electrodes for supercapacitors. J. Energy Storage *72*, 108513. https://doi.org/10.1016/j.est.2023.108513.
34. Haralakal, K.K., Ashwini, M., Goudar, G.D., Achappa, S., Achappa, S., Chikkatti, B.S., Banapurmath, N.R., and Sajjan, A.M. (2025). Exploring the nature of nano bacterial cellulose-poly (vinyl alcohol) as a composite packaging material. Next Nanotechnol. *7*, 100099. https://doi.org/10.1016/j.nxnano.2024.100099.
35. Chikkatti, B.S., Sajjan, A.M., Banapurmath, N.R., and Ayachit, N.H. (2023). Graphene-Doped hydrogels promoting ionic conductivity in gel-valve-regulated lead acid batteries. Langmuir *39*, 17232–17239. https://doi.org/10.1021/acs.langmuir.3c02285.
36. Yang, T., Xu, X., Chen, S., Yang, Y., Li, F., Fan, W., Wu, Y., Zhao, J., Liu, J., and Huo, Y. (2025). A Lithiophilic Donor–Acceptor Polymer Modified Separator for High-Performance Lithium Metal Batteries. Angew. Chem. Int. Ed. Engl. *64*, e202420973. https://doi.org/10.1002/anie.202420973.
37. Xiao, Z., Li, L., Tang, Y., Cheng, Z., Pan, H., Tian, D., and Wang, R. (2018). Covalent organic frameworks with lithiophilic and sulfiphilic dual linkages for cooperative affinity to polysulfides in lithium-sulfur batteries. Energy Storage Mater. *12*, 252–259. https://doi.org/10.1016/j.ensm.2018.01.018.
38. Yang, Z., Dang, Y., Zhai, P., Wei, Y., Chen, Q., Zuo, J., Gu, X., Yao, Y., Wang, X., Zhao, F., et al. (2022). Single-atom reversible lithiophilic sites toward stable lithium anodes. Adv. Energy Mater. *12*, 2103368. https://doi.org/10.1002/aenm.202103368.
39. Song, L., Wang, R., Niu, K., Liu, Y., Kou, J., Song, H., Zhang, J., and Wang, Q. (2021). Design, synthesis, characterization, and surface activities of comb-like polymeric fluorinated surfactants with short fluoroalkyl chains. Colloids Surf. A: Physicochem. Eng. Aspects *609*, 125666. https://doi.org/10.1016/j.colsurfa.2020.125666.
40. Li, M., Rakov, D.A., Fan, Y., Wang, C., Wang, C., Yuwono, J.A., Xia, S., Mao, J., and Guo, Z. (2025). Balancing Solvation Ability of Polymer and Solvent in Gel Polymer Electrolytes for Efficient Lithium Metal Batteries. Angew. Chem. Int. Ed. Engl. *64*, e202513450. https://doi.org/10.1002/anie.202513450.
41. Wang, Y., Zheng, C., Xie, W., Liu, X., Lu, Y., Hou, Y., Ma, T., Yan, Z., and Chen, J. (2024). Ether-Modified Nonflammable Phosphate Enabling Anion-Rich Electrolyte for High-Voltage Lithium Metal Batteries. Adv. Mater. *36*, e2312302. https://doi.org/10.1002/adma.202312302.
42. Wang, M., Zheng, M., Lu, J., and You, Y. (2024). High-entropy electrolyte toward battery working under extreme conditions. Joule *8*, 2467–2482. https://doi.org/10.1016/j.joule.2024.07.019.
43. Yang, Y., Wang, X., Zhu, J., Tan, L., Li, N., Chen, Y., Wang, L., Liu, Z., Yao, X., Wang, X., et al. (2024). Dilute Electrolytes with Fluorine-Free Ether Solvents for 4.5 V Lithium Metal Batteries. Angew. Chem. Int. Ed. Engl. *63*, e202409193. https://doi.org/10.1002/anie.202409193.
44. Liu, Y., Jin, Z., Liu, Z., Xu, H., Sun, F., Zhang, X.Q., Chen, T., and Wang, C. (2024). Regulating the Solvation Structure in Polymer Electrolytes for High-Voltage Lithium Metal Batteries. Angew. Chem. Int. Ed. Engl. *63*, e202405802. https://doi.org/10.1002/anie.202405802.
45. Wang, C., Liu, S., Xu, H., Wang, X., Tian, G., Fan, F., Liu, P., Wang, S., Zeng, C., and Shu, C. (2024). Adjusting Li^+ Solvation Structures via Dipole–Dipole Interaction to Construct Inorganic-Rich Interphase for High-Performance Li Metal Batteries. Small *20*, e2308995. https://doi.org/10.1002/smll.202308995.
46. Chen, W., Park, J.-S., Kwon, C., Plaza-Rivera, C.O., Hsu, C.-W., Phong, J.K., Kilgallon, L.J., Wang, D., Dai, T., Kim, S.Y., et al. (2025). Hybrid solvating electrolytes for practical sodium-metal batteries. Joule *9*, 101811. https://doi.org/10.1016/j.joule.2024.101811.
47. Chikkatti, B.S., Sajjan, A.M., Banapurmath, N.R., Ayachit, N.H., Jazaa, Y., Yunus Khan, T.M., and Umarfarooq, M.A. (2025). Novel polymer gel electrolytes comprising montmorillonite embedded in sodium alginate and their electrochemical performance for future lead acid batteries. New J. Chem. *49*, 3654–3660. https://doi.org/10.1039/D4NJ05557H.

Please cite this article in press as: Cong et al., Gel electrolyte featuring parasitic salt-phobic network enables anode-free lithium batteries with long cycle life and enhanced thermal stability, Joule (2025), https://doi.org/10.1016/j.joule.2025.102296

48. Adams, B.D., Zheng, J., Ren, X., Xu, W., and Zhang, J.G. (2018). Accurate determination of coulombic efficiency for lithium metal anodes and lithium metal batteries. Adv. Energy Mater. *8*, 1702097. https://doi.org/10.1002/aenm.201702097.

49. Ma, X., Zhang, D., Fu, H., Rao, A.M., Zhou, J., Fan, L., and Lu, B. (2025). Energy band-engineered solid electrolyte interphase for stable potassium-ion batteries. Joule *9*, 101952. https://doi.org/10.1016/j.joule.2025.101952.

50. Ma, S., Zhao, J., Xiao, H., Gao, Q., Li, F., Song, C., and Li, G. (2025). Modulating the Inner Helmholtz Plane towards Stable Solid Electrolyte Interphase by Anion-π Interactions for High-Performance Anode-Free Lithium Metal Batteries. Angew. Chem. Int. Ed. Engl. *64*, e202412955. https://doi.org/10.1002/anie.202412955.

51. Liu, L., and Wang, J. (2025). From cell to atomic level: understanding the degradation in 99% coulombic efficiency and 450 Wh kg-1 anode-free pouch cells. J. Am. Chem. Soc. *147*, 41342–41354. https://doi.org/10.1021/jacs.5c09562.

52. Choi, I.R., Chen, Y., Shah, A., Florian, J., Serrao, C., Holoubek, J., Lyu, H., Zhang, E., Lee, J.H., Lin, Y., et al. (2025). Asymmetric ether solvents for high-rate lithium metal batteries. Nat. Energy *10*, 365–379. https://doi.org/10.1038/s41560-025-01716-w.

53. Shi, J., Koketsu, T., Zhu, Z., Yang, M., Sui, L., Liu, J., Tang, M., Deng, Z., Liao, M., Xiang, J., et al. (2024). In situ p-block protective layer plating in carbonate-based electrolytes enables stable cell cycling in anode-free lithium batteries. Nat. Mater. *23*, 1686–1694. https://doi.org/10.1038/s41563-024-01997-8.

54. Gervillié-Mouravieff, C., Ah, L., Liu, A., Huang, C.-J., and Meng, Y.S. (2024). Deciphering the impact of the active lithium reservoir in anode-free pouch cells. ACS Energy Lett. *9*, 1693–1700. https://doi.org/10.1021/acsenergylett.4c00457.

55. Mao, M., Ji, X., Wang, Q., Lin, Z., Li, M., Liu, T., Wang, C., Hu, Y.-S., Li, H., Huang, X., et al. (2023). Anion-enrichment interface enables high-voltage anode-free lithium metal batteries. Nat. Commun. *14*, 1082. https://doi.org/10.1038/s41467-023-36853-x.

56. Zhang, Z., Luo, H., Liu, Z., Wang, S., Zhou, X., and Liu, Z. (2022). A chemical lithiation induced Li 4.4 Sn lithiophilic layer for anode-free lithium metal batteries. J. Mater. Chem. A *10*, 9670–9679. https://doi.org/10.1039/d2ta00167e.

57. Zhang, S., Li, R., Hu, N., Deng, T., Weng, S., Wu, Z., Lu, D., Zhang, H., Zhang, J., Wang, X., et al. (2022). Tackling realistic Li^+ flux for high-energy lithium metal batteries. Nat. Commun. *13*, 5431. https://doi.org/10.1038/s41467-022-33151-w.

58. Niu, C., Liu, D., Lochala, J.A., Anderson, C.S., Cao, X., Gross, M.E., Xu, W., Zhang, J.-G., Whittingham, M.S., Xiao, J., et al. (2021). Balancing interfacial reactions to achieve long cycle life in high-energy lithium metal batteries. Nat. Energy *6*, 723–732. https://doi.org/10.1038/s41560-021-00852-3.

59. Lin, L., Suo, L., Hu, Y.S., Li, H., Huang, X., and Chen, L. (2021). Epitaxial induced plating current-collector lasting lifespan of anode-free lithium metal battery. Adv. Energy Mater. *11*, 2003709. https://doi.org/10.1002/aenm.202003709.

60. Lin, L., Qin, K., Zhang, Q., Gu, L., Suo, L., Hu, Y.S., Li, H., Huang, X., and Chen, L. (2021). Li-Rich Li_2 [$Ni_{0.8}Co_{0.1}Mn_{0.1}$] O_2 for Anode-Free Lithium Metal Batteries. Angew. Chem. Int. Ed. *60*, 8289–8296. https://doi.org/10.1002/anie.202017063.

61. Yim, T., Kim, K., Hassig, M.Q., Nedsaengtip, J., Zhang, T., Jamkar, S., Li, C.Y., and Kalra, V. (2025). Lithium-Nitrate-Containing Gel Polymer Electrolyte for Carbonate-Based Anode-Free Lithium Metal Batteries. ACS Appl. Mater. Interfaces *17*, 37851–37862. https://doi.org/10.1021/acsami.5c03252.

62. Agnihotri, T., Ahmed, S.A., Tamilarasan, E.B., Hasan, R., Hotasi, B.T., Bezabh, H.K., Suwito, S., Nikodimos, Y., Jiang, S.-K., Shitaw, K.N., et al. (2024). Anion-trapping composite gel electrolyte for safer and more stable anode-free lithium-metal batteries. Chem. Eng. J. *484*, 149608. https://doi.org/10.1016/j.cej.2024.149608.

63. Lin, Y.-H., Wu, L.-T., Zhan, Y.-T., Jiang, J.-C., Lee, Y.-L., Jan, J.-S., and Teng, H. (2023). Self-assembly formation of solid-electrolyte interphase in gel polymer electrolytes for high performance lithium metal batteries. Energy Storage Mater. *61*, 102868. https://doi.org/10.1016/j.ensm.2023.102868.

64. Chikkatti, B.S., Sajjan, A.M., and Banapurmath, N.R. (2023). The state of understanding of the electrochemical behaviours of a valve-regulated lead–acid battery comprising manganese dioxide-impregnated gel polymer electrolyte. Mater. Adv. *4*, 6192–6198. https://doi.org/10.1039/d3ma00563a.

65. Li, Z., Li, A., Zhang, H., Lin, R., Jin, T., Cheng, Q., Xiao, X., Lee, W.-K., Ge, M., Zhang, H., et al. (2020). Interfacial engineering for stabilizing polymer electrolytes with 4V cathodes in lithium metal batteries at elevated temperature. Nano Energy *72*, 104655. https://doi.org/10.1016/j.nanoen.2020.104655.

66. Chikkatti, B.S., Sajjan, A.M., Kalahal, P.B., and Banapurmath, N.R. (2023). Insight into the performance of valve-regulated lead-acid battery using sodium salt of poly (4-styrene sulfonic acid-co-maleic acid)-poly (vinyl alcohol) gel electrolyte. J. Energy Storage *72*, 108261. https://doi.org/10.1016/j.est.2023.108261.

67. Sau, S., Panda, M.R., Barik, G., Gautam, M., Adil, M., Jha, S.N., and Mitra, S. (2023). Unravelling redox phenomenon and electrochemical stability of $Li_{1.6}Al_{0.5}Ge_{1.5}P_{2.9}Si_{0.1}O_{12}$ solid electrolyte against Li metal and silicon anodes for advanced solid-state batteries. Mater. Today Energy *38*, 101445. https://doi.org/10.1016/j.mtener.2023.101445.

68. Li, Y., Li, Y., Pei, A., Yan, K., Sun, Y., Wu, C.-L., Joubert, L.-M., Chin, R., Koh, A.L., Yu, Y., et al. (2017). Atomic structure of sensitive battery materials and interfaces revealed by cryo–electron microscopy. Science *358*, 506–510. https://doi.org/10.1126/science.aam6014.

69. Liu, J., Hao, W., Fang, M., Chen, X., Dong, Y., Chen, Y., Wang, Z., Yue, X., and Liang, Z. (2024). Screening of F-containing electrolyte additives and clarifying their decomposition routes for stable Li metal anodes. Nat. Commun. *15*, 9356. https://doi.org/10.1038/s41467-024-53807-z.

70. Yang, Y., Wang, J., Li, Z., Yang, Z., Wang, B., and Zhao, H. (2024). Constructing LiF-Dominated Interphases with Polymer Interwoven Outer Layer Enables Long-Term Cycling of Si Anodes. ACS Nano *18*, 7666–7676. https://doi.org/10.1021/acsnano.4c00998.

71. Xiang, J., Zhang, Y., Zhang, B., Yuan, L., Liu, X., Cheng, Z., Yang, Y., Zhang, X., Li, Z., Shen, Y., et al. (2021). A flame-retardant polymer electrolyte for high performance lithium metal batteries with an expanded operation temperature. Energy Environ. Sci. *14*, 3510–3521. https://doi.org/10.1039/d1ee00049g.